Journal of Electroanalytical Chemistry 849 (2019) 113368

Contents lists available at ScienceDirect

Journal of Electroanalytical Chemistry

journal homepage: www.elsevier.com/locate/jelechem

# Synthesis of $CaCr_2O_4$/carbon nanoplatelets from non-condensable pyrolysis gas of plastics for oxygen reduction reaction and charge storage

Andrei Veksha [a,*], James Guo Sheng Moo [a], Vida Krikstolaityte [a,b], Wen-Da Oh [a,c], W.D. Chanaka Udayanga [a], Apostolos Giannis [a,d], Grzegorz Lisak [a,b,**]

[a] Residues and Resource Reclamation Centre (R3C), Nanyang Environment and Water Research Institute (NEWRI), Nanyang Technological University, 1 Cleantech Loop, CleanTech One, Singapore 637141, Singapore
[b] School of Civil and Environmental Engineering, Nanyang Technological University, 50 Nanyang Avenue, Singapore 639798, Singapore
[c] School of Chemical Sciences, Universiti Sains Malaysia, Penang 11800, Malaysia
[d] School of Environmental Engineering, Technical University of Crete (TUC), University Campus, Chania 73100, Greece

ARTICLE INFO

*Article history:*
Received 20 May 2019
Received in revised form 28 July 2019
Accepted 7 August 2019
Available online 8 August 2019

*Keywords:*
Carbon nanoplatelets
Chromium composite
Electrochemical capacitance
Heterogeneous electron transfer
Oxygen reduction reaction

ABSTRACT

An integrated pyrolysis and chemical vapor deposition using $CaCrO_4$ as a precursor were applied to convert mixed plastics into a nanocomposite comprising $CaCr_2O_4$ and carbon nanoplatelets ($CaCr_2O_4$/CNPs). During pyrolysis, plastics were decomposed into oil and non-condensable gas. While reacting with the precursor, non-condensable pyrolysis gas containing hydrocarbons and $H_2$ played a dual role: (1) provided carbon for nanoplatelets growth and (2) facilitated reduction of Cr(VI) to Cr(III). Cyclic voltammetry demonstrated the synergistic effect of $CaCr_2O_4$ and CNPs on the heterogeneous electron transfer rate. The nanocomposite showed good performance as an electrocatalyst for oxygen reduction reaction increasing current density and reducing overpotential to −0.27 V vs Ag/Ag/KCl (sat.) at 0.06 mA $cm^{-2}$. Furthermore, the nanocomposite exhibited a specific electrochemical capacitance as high as 60 F $g^{-1}$ at 2 A $g^{-1}$ and 67% stability over 3000 cycles, demonstrating the capability of electrode for fast charge/discharge, long cycling life and high reversibility.



## 1. Introduction

Transition metal oxides have been widely explored as electrode materials for energy storage devices and fuel cells. Due to electrochemical pseudocapacitance originating from redox reactions occurring at the metal oxide–electrolyte interface, transition metal oxides have high theoretical specific electrochemical capacitances compared to carbon materials and its derivatives (e.g., 1370 F $g^{-1}$ for $MnO_2$, 3560 F $g^{-1}$ for $Co_3O_4$, 2584 F $g^{-1}$ for NiO against 526 F $g^{-1}$ of graphene) [1–4]. Owing to the low-cost and high availability, transition metal oxides have been also investigated for the possible application in electrocatalysis, instead of relatively expensive precious metals [5,6]. Nanostructured oxides of Mn, Ni, Co, Fe and other metals were reported to catalyze oxygen reduction (ORR) and evolution (OER) reactions [5,6]. ORR plays an essential role as a cathodic half-cell in proton exchange membrane fuel cells [7], while OER is an important half-cell reaction for water splitting [8]. Furthermore, both OER and ORR are employed in rechargeable air-metal batteries [9], which have three to thirty times greater energy density than those of lithium-ion batteries and can potentially be used as energy storage devices [10]. The high electrochemical capacitance and the performance of metal oxides as electrocatalysts, however, are limited by the low electrical conductivity and the particle agglomeration. Binary metal oxides and metal oxide–carbon composites were reported to exhibit better electrochemical performance compared to single metal oxides, which is attributed to the changes in chemical composition, such as introduction of oxygen vacancies and incorporation of conductive carbon materials [4,6,10].

For electrochemical applications, the promising types of binary oxide systems are metal chromite spinels as they possess high chemical stability and can be used either directly or as a composite with carbon based materials [11–14]. $NiCr_2O_4$ synthesized by co-precipitation of Ni (II) and Cr(III) salts have demonstrated high-performance as an electrode material for an electrochemical supercapacitor application [11]. Nanocomposites containing $CoCr_2O_4$ and carbon nanosheets grown by a facile one-step molten salt calcination method have exhibited good electrocatalytic activity and durability during OER [12]. $ZnCr_2O_4$ and multi-walled carbon nanotubes composite synthesized using hydrothermal method followed by calcination at 500 °C showed good performance as an enzyme-free sensor for monitoring $H_2O_2$ content in aqueous solutions [13]. $MnCr_2O_4$/$Mn^{II}Mn^{III}_2O_4$/carbon and $CoCr_2O_4$/

* Corresponding author.
** Correspondence to: Residues and Resource Reclamation Centre (R3C), Nanyang Environment and Water Research Institute (NEWRI), Nanyang Technological University, 1 Cleantech Loop, CleanTech One, Singapore 637141, Singapore.
*E-mail addresses:* aveksha@ntu.edu.sg (A. Veksha), g.lisak@ntu.edu.sg (G. Lisak).

https://doi.org/10.1016/j.jelechem.2019.113368
1572-6657/

carbon nanocomposites prepared by annealing of Mn—Cr and Co—Cr coordination compounds at 350 °C in air, respectively, demonstrated high specific electrochemical capacitance [14].

Despite the proof that transition metal chromites either independently or as composites with carbon nanostructures can serve as high performance electroactive materials, there is lack of evidence regarding the performance of non-transition metal chromites. To address this issue, in the present work, a novel composite comprising $CaCr_2O_4$ and carbon nanoplatelets ($CaCr_2O_4$/CNPs) was synthesized and tested. Two stage thermal process was applied for the synthesis of the nanocomposite material. In the first stage, plastic mixture, simulating the composition of mixed plastic waste, was converted into oil and non-condensable pyrolysis gas. While oil can be utilized in boilers and internal combustion engines, non-condensable pyrolysis gas (representing 10–90% of product yields [15,16]) is typically burnt [17]. Upcycling of non-condensable pyrolysis gas into carbon-based electrode materials can substantially reduce the carbon footprint of plastic pyrolysis and serve as a source of hydrocarbons for the synthesis. Therefore, in the second stage, non-condensable pyrolysis gas was converted via chemical vapor deposition into carbon nanostructures over the chromium containing precursor. The produced nanocomposite was characterized using voltammetry and electrochemical impedance spectroscopy to investigate heterogeneous electron transfer, and applied as an electrode material for electrocatalytic ORR and charge storage in supercapacitors. The capabilities of plastic-derived $CaCr_2O_4$/CNPs to facilitate ORR and sustain long-term electrochemical capacitance are discussed.

## 2. Materials and methods

### 2.1. Synthesis

The precursor for synthesis of $CaCr_2O_4$/carbon nanoplatelets (CNPs) denoted as Cr—Ca was prepared by impregnation method using calcium carbonate (98.5%, Reagent and Fine Chemicals) and chromium (III) nitrate nonahydrate (98.5% pure, Alfa Aesar). Chromium(III) nitrate nonahydrate (7.8 g) was dissolved in 100 mL of water and mixed with calcium carbonate (19 g) to obtain a Cr:Ca molar ratio of 1:10. A lower than stoichiometric content of Cr was selected to maintain the chromium(III) nitrate in the dispersed state and avoid particle agglomeration during the synthesis of nanocomposite. The solvent was evaporated in a rotary evaporator. The remaining powder was dried overnight in an oven at 55 °C, calcined in air at 750 °C for 3 h (heating rate 2 °C $min^{-1}$) and sieved to 63–212 μm particle size.

The plastic mixture containing typical polymer present in plastic waste, namely 40% low density polyethylene (LDPE, PTT Global Chemical Public Co. Ltd., Thailand), 40% polypropylene (PP, Sinopec, China), 10% polystyrene (PS, Formosa Plastics Corp., Taiwan) and 10% polyvinyl chloride (PVC, Hop Fu Plastics Ltd., China), was used for the experiments. The synthesis of nanocomposite was carried out in a two-stage pyrolysis and chemical vapor deposition process (Fig. S1). Horizontal tubular quartz reactor (i.d. 53 mm) was applied for pyrolysis of the plastic mixture (1.86 g) producing condensable oil and non-condensable gas. Condensable products were separated by a condenser at ambient temperature, while non-condensable gas passed through the vertical reactor (i.d. 17 mm) loaded with Cr—Ca. The reactor had a gas permeable frit to support Cr—Ca in the middle of the heating zone of a furnace. The amount of loaded Cr—Ca was 0.5 g. Once the plastics and Cr—Ca were loaded into the reactors, the reactor with Cr—Ca was heated to the synthesis temperature (500, 600 or 700 °C) at the heating rate of 15 °C $min^{-1}$ in 100 mL $min^{-1}$ $N_2$ flow. When the synthesis temperature was reached, the reactor with plastics was heated to 600 °C at the heating rate of 10 °C $min^{-1}$ and then maintained at 600 °C for 30 min to decompose the plastics. After the synthesis, the reactors were cooled in $N_2$, the produced black product was washed with 3 M HCl acid and dried at 105 °C prior to characterization. In order to obtain a CNPs-free sample, the $CaCr_2O_4$/CNPs nanocomposite was calcined in air at 500 °C for 2 h.

The non-condensable pyrolysis gas passed through two traps containing isopropanol to capture $C_{6+}$ aromatic hydrocarbons released during the decomposition of plastics. The purified gas was collected into gas bags and characterized by a gas chromatograph with two thermal conductivity detectors for $H_2$, CO, $CO_2$ and $N_2$ concentration and one flame ionization detector for $C_1$-$C_5$ hydrocarbons. The volume of each gaseous component was calculated using $N_2$ volume in non-condensable pyrolysis gas as an internal standard. To analyze $C_{6+}$ hydrocarbons captured in isopropanol, solvent from both traps was combined in a volumetric flask and topped up until the mark. Analysis of dissolved hydrocarbon species was carried out using gas chromatography–mass spectrometry (GC–MS, HP7890 GC with a 5975I MS, Agilent) equipped with a HP-INNOWAX capillary column (I.D. 0.250 mm and a film thickness 0.25 μm). Toluene $d_8$ was used as the internal standard during the analysis.

### 2.2. Characterization of material structure

The materials were characterized using field emission scanning electron microscopy (FESEM, JEOL JSM-7600F) equipped with the energy dispersive X-ray spectroscope (EDS, Oxford Xmax80 LN2 Free), transmission electron microscopy (TEM, JEOL JEM-1400 and JEM-2010), X-ray diffraction analysis (XRD, Bruker AXS D8 Advance), Raman spectroscopy (XploRA PLUS with a 532 nm laser, Horiba Scientific), X-ray photoelectron spectroscopy (XPS, Kratos Axis Supra) and $N_2$ adsorption and desorption isotherms at −196 °C (Quantachrome Autosorb-1 Analyzer). Specific surface area and pore size distribution were calculated from $N_2$ adsorption data applying the BET model and quenched solid density functional theory (QSDFT) equilibrium model, which takes into account heterogeneity of surface of carbonaceous materials [18]. QSDFT modeling was conducted assuming slit pore geometry of carbon in nanocomposite.

Temperature programmed oxidation was conducted in a thermogravimetric analyzer STA 449 F3 Jupiter (Netzsch Group). 10 mg of nanocomposite was loaded into an $Al_2O_3$ crucible, dried in air (250 mL $min^{-1}$) at 105 °C to remove moisture and then heated in air at to 1000 °C (15 °C $min^{-1}$).

### 2.3. Electrochemical testing

*N*,*N*-dimethylformamide (DMF), potassium ferrocyanide trihydrate [$K_4Fe(CN)_6 \cdot 3H_2O$], potassium ferricyanide [$K_3Fe(CN)_6$], potassium chloride, potassium hydroxide, 20 wt% platinum on graphitised carbon and concentrated sulphuric acid (95–98%) were purchased from Sigma Aldrich.

All electrochemical measurements, namely, cyclic voltammetry (CV), linear sweep voltammetry (LSV), electrochemical impedance spectroscopy (EIS), and charge/discharge (CD) measurements by chronopotentiometry were conducted using Interface 1000 Potentiostat (Gamry, USA) equipped with a three-electrode electrochemical cell consisted of a Pt mesh as a counter electrode, Ag/AgCl/KCl (sat.) (ALS, Japan) as a reference electrode and a glassy carbon (GC) disk as a working electrode (CH Instruments, USA) (the working surface area of 0.07 $cm^2$). 0.05 μm alumina and micropolishing pad were obtained from ALS, Japan. The electrodes were used as received and were not recalibrated. All electrochemical experiments were performed at ambient temperature (24–25 °C) in a voltammetric cell (5 mL) with no agitation. The electrolyte was bubbled with air and $N_2$ for 20 min to reach air-saturation and $N_2$-saturation, respectively. Before the usage, the GC electrodes were polished using 0.05 μm polishing alumina slurry on a polishing pad and rinsed with absolute ethanol followed by washing with ultra-high quality (UHQ) water. Two different approaches were used for the preparation of $CaCr_2O_4$/CNPs dispersions which were used to modify GC electrodes. For electron transfer

characterization by CV and EIS in mild conditions, specifically, in 5 mM potassium hexacyanoferrate (III)/(II) ($Fe(CN)_6^{3-/4-}$) containing 100 mM KCl, 1 mg $mL^{-1}$ of $CaCr_2O_4$/CNPs were dispersed in chitosan solution (0.1% of chitosan in acetic acid) using a probe sonicator with a diameter of 3 mm as described elsewhere [19]. Sonication was performed for 2 min using 3 s pulses with 1 s intervals at amplitude of 20%. GC electrodes were modified by drop-casting two portions of 3 μL of $CaCr_2O_4$/CNPs dispersion on a GC electrode. The second drop was added after 30 min, making sure the first drop had dried. CVs were performed at 50 mV $s^{-1}$ scan rate from −0.2 to 0.6 V. Five cycles were measured and the second cycle was chosen as the representative one due to the negligible differences between the data obtained during second and fifth cycles. EIS was carried out in the frequency range from 0.1 Hz to 100 kHz at an open circuit potential with an alternating current amplitude of 10 mV. Open circuit potential was stabilized for 10 s.

Oxygen reduction reaction (ORR) and specific electrochemical capacitance (EC) evaluation were performed using 0.1 M KOH and 1 M $H_2SO_4$ solutions, respectively. For these tests, the second dispersion protocol described by Maharjan et al. was employed to modify GC electrode with $CaCr_2O_4$/CNPs [20]. 5 mg $mL^{-1}$ of the $CaCr_2O_4$/CNPs were dispersed in *N*,*N*-dimethylformamide and sonicated in an ultrasound bath for 30 min to obtain a homogeneous dispersion. 1 μL of the dispersion was deposited on a GC electrode and dried under an incandescent lamp for 10 min. ORR tests were performed by LSV (sweeping rate 5 mV $s^{-1}$) with an air-saturated and $N_2$-saturated electrolytes. EC was evaluated by using both CVs at different scan rates (10–200 mV $s^{-1}$) and charge/discharge measurements applying a constant current density between 1 and 20 A $g^{-1}$ in 1.0 M $H_2SO_4$ electrolyte. The electrolyte was bubbled with $N_2$ for 20 min to reach $N_2$-saturation prior to the electrochemical characterization. The corresponding specific EC of the material was determined from the CD curve using the equation given below:

$$EC = \frac{i \times \Delta t}{\Delta v \times m} \quad (1)$$

where $i$ is the discharge current, $\Delta t$ is the time taken for the discharge to occur in the potential window, $\Delta v$ is the potential window and $m$ is the mass of the active electrode material [21]. $\Delta t/\Delta v$ was calculated from the second half slope of the CD curve. Cycling stability was measured with the same setup at 2 A $g^{-1}$.

## 3. Results and discussion

### 3.1. $CaCr_2O_4$/CNPs synthesis

Fig. 1 shows the XRD pattern of the Cr—Ca precursor used for the synthesis of $CaCr_2O_4$/CNPs from non-condensable pyrolysis gas. The XRD pattern contains well-defined peaks which can be indexed to crystalline $CaCO_3$, $Ca(OH)_2$, CaO and $CaCrO_4$ (chromatite) phases. The CaO is formed from the decomposition of $CaCO_3$ support during thermal treatment, while $Ca(OH)_2$ is formed from CaO and moisture in air during handling and XRD analysis. During calcination, Cr(III) was oxidized to Cr(VI) as suggested by the formation of $CaCrO_4$. Similar results were reported when chromium(III) nitrate was used for the synthesis of chromium-based catalysts supported on $Al_2O_3$ [22]. At loadings up to 9% by mass, $CrO_3$ was the dominant chromium species while at higher loadings $CrO_3$ was partially reduced to $Cr_2O_3$. Due to the acidic nature, $CrO_3$ can react with calcium compounds during the calcination stage producing $CaCrO_4$.

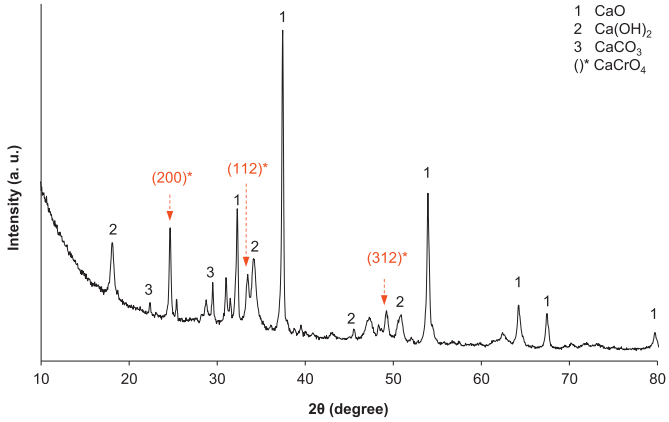


**Fig. 1.** XRD pattern of the Cr—Ca precursor.

The yields and ultimate analyses of nanocomposites prepared at three synthesis temperatures are summarized in Table 1. An increase in synthesis temperature from 500 to 700 °C increased the yield of produced nanocomposite material nearly 2.3 times from 6.2 to 14.1% per Cr—Ca mass. The ultimate analysis confirmed the presence of 8.5–13.6% C and 1.2–2.9% H in the synthesized materials (depending on the temperature of chemical vapor deposition), while N content was negligible. To identify the type of hydrocarbon compounds in the non-condensable pyrolysis gas acting as precursors for carbon deposition over Cr—Ca, the $C_1$-$C_5$ gases and $C_{6+}$ hydrocarbons were analyzed by GC and GC–MS, respectively. Fig. 2a depicts the volumes of $C_1$-$C_5$ hydrocarbons and $H_2$ in the non-condensable pyrolysis gas after the treatment in the absence and presence of Cr—Ca at 700 °C (i.e. at the temperature that resulted in the highest yield of nanocomposite material). Both gases contained substantial quantities of methane, ethane, propane, ethylene, propylene and $C_4$ alkenes. Traces of other compounds, such as $C_4$ and $C_5$ alkanes, dienes and acetylenes, were also present. The total yields of collected $C_1$-$C_5$ hydrocarbons produced during pyrolysis of plastic mixture after the treatment in the presence and absence of Cr—Ca were 14.8 ± 0.7 and 15.0 ± 1.1% per mass of feedstock, respectively (the data are presented as averages ± standard deviations of three runs). The differences in the volumes of hydrocarbon gases were also within the statistical error, indicating that there was no significant decomposition of $C_1$-$C_5$ hydrocarbons. On the other hand, after the gas treatment in the presence of Cr—Ca, the volume of $H_2$ increased, suggesting the deposition of carbon from other carbonaceous precursors via the following reaction:

$$C_xH_y = xC + 0.5yH_2 \quad (2)$$

Since no decomposition of $C_1$-$C_5$ hydrocarbons was observed, $C_{6+}$ hydrocarbons were the most likely precursors. Fig. 2b shows a representative GC–MS chromatogram of isopropanol solution collected in the absence of Cr—Ca at 700 °C. 13 peaks with retention times between 2.8 and 7.5 min were observed and are attributed to $C_{6+}$ hydrocarbons, one of which is the internal standard (i.e. toluene $d_8$) added for quality control. The assignment and decomposition of these compounds in the presence of Cr—Ca at 700 °C are summarized in Table 2. All the identified species were cyclic hydrocarbons (aromatic and non-aromatic) containing double carbon bonds. Benzene and toluene were the most stable species and did not decompose over Cr—Ca. The decomposition of other species was between 11 and 100%, explaining the release of $H_2$ and formation of carbon in the nanocomposites.

**Table 1**
Yields and ultimate analyses of nanocomposites prepared at different temperatures.

| Temperature (°C) | Yield (wt%)[a] | C (wt%) | H (wt%) | N (wt%) |
|---|---|---|---|---|
| 500 | 6.2 | 13.6 | 2.9 | 0.1 |
| 600 | 11.9 | 8.5 | 2.3 | 0 |
| 700 | 14.1 | 11.1 | 1.2 | 0.1 |

[a] Calculated as (mass of nanocomposite after HCl washing/mass of Cr—Ca) × 100%.

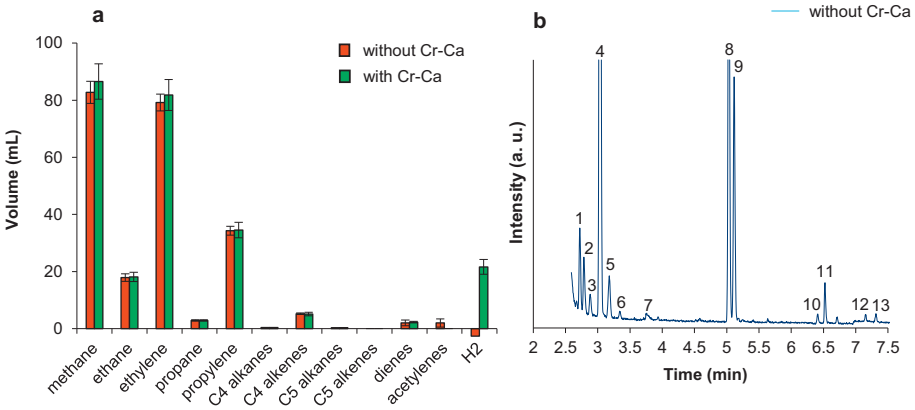


**Fig. 2.** (a) $C_1$-$C_5$ hydrocarbons (the data are presented as averages ± standard deviation of three runs) and (b) $C_{6+}$ hydrocarbons in the product gas (700 °C).

### 3.2. Structure of $CaCr_2O_4$/CNPs

The physicochemical and electrochemical properties of the nanocomposite synthesized at 700 °C were characterized as the material produced at this temperature had the highest yield. Fig. 3a depicts the temperature programmed oxidation profile. The loss of ~28% of mass during thermal treatment in air at temperatures between 270 and 470 °C was observed and is attributed to the partial combustion of the material (i.e. carbon). The mass of the remaining inorganic fraction (~72%) did not change significantly up to 1000 °C, indicating high resistance to oxidation of the formed $CaCr_2O_4$. The Raman spectra in Fig. 3b contains peaks at ~1350 $cm^{-1}$ (D-band) and 1580 $cm^{-1}$ (G-band) corresponding to deposited carbon [23]. The presence of both peaks indicates defective structure of the material and low graphitization degree, which are typical to many carbon materials synthesized via chemical vapor deposition technique [24–27]. The shoulder at 1100 $cm^{-1}$ corresponds to symmetric $CO_3^{2-}$ stretching in metal carbonates [27]. This indicates that most likely, carbonate-ions are present as an impurity on the surface of material or were incorporated into the structure of nanocomposite upon synthesis due to the utilization of $CaCO_3$ support. The Raman peak at ~600 $cm^{-1}$ corresponds to vibrations in $Cr_2O_4^{2-}$ [28,29].

According to Fig. 3c, the nanocomposite has broad XRD peaks that could be attributed to α-$CaCr_2O_4$ spinel, which has the orthorhombic structure with *Pmmn* space group. In oxygen free atmosphere, the conversion of $CaCrO_4$ into $CaCr_2O_4$ starts above ~900 °C [30], which is ≥200 °C higher that the temperatures utilized in this study. The lower temperature required for $CaCr_2O_4$ synthesis could be attributed to the presence of hydrocarbons and $H_2$ in the gas, which facilitate the reduction of Cr(VI) to Cr(III) [31]:

$$2CaCrO_4 + 3H_2 = CaCr_2O_4 + CaO + 3H_2O \quad (3)$$

The absence of graphite peaks in XRD pattern at 27° and 43° (Fig. 3c) suggests non-crystalline structure of CNPs [32]. The small broad peaks emerging in the regions of 50–60° and 70–80° could be attributed to unidentified impurities, which have low crystallinity and/or present at low concentrations. Energy dispersive X-ray spectroscopy (EDS) spectrum confirms the presence of Ca and Cr in the synthesized nanocomposite (Fig. S2). Only traces of chlorine were identified in the sample, which can originate from chlorine species released during pyrolysis of PVC and/or from HCl used for acid washing. According to EDS, the atomic Ca:Cr ratio was 1:7.4, indicating that other non-crystalline chromium compounds can be present in the $CaCr_2O_4$/CNPs sample. As suggested by Cr 2p core level XPS spectrum (Fig. S3), Cr 2p3/2 had binding energy of 577 eV, corresponding to Cr(III) species [11]. According to $N_2$ adsorption isotherm shown in Fig. 3d, the nanocomposite is a porous material with total pore volume of 0.42 mL $g^{-1}$ containing both micro- ($P/P_0 < 0.1$) and mesopores ($0.1 < P/P_0 < 0.95$). The larger $N_2$ adsorption at $P/P_0 > 0.1$ suggests that mesopores predominate in the synthesized material. This is also evident from the pore size distribution (Fig. 3e) illustrating that the majority of pores is in the mesopore range between 2 and 16 nm. The specific surface areas of nanocomposite calculated using BET and QSDFT models are 120 and 136 $m^2$ $g^{-1}$, respectively, suggesting good agreement between the models used for the characterization of nanocomposite.

Fig. 4 illustrates FESEM and TEM images of the synthesized $CaCr_2O_4$/CNPs nanocomposite (700 °C). Two types of structures can be identified in the images. The major part of the nanocomposite comprises flat plates with thicknesses 4–25 nm as shown in Fig. 4a and b. Side views in Fig. 4c and d suggest that the plates consist of layered material with ordered arrangement of atoms and are probably attributed to $CaCr_2O_4$, which is the main crystalline compound in the nanocomposite. The thickness of layers in plates was approximately 0.6 nm (Fig. 4d). These plates are surrounded by the second type of material (Fig. 4e and f), which appears to be carbon and resembles the morphology of carbon nanoplatelets [33].

The data presented in Figs. 3 and 4 demonstrate that the proposed synthesis route is a viable method for fabrication of $CaCr_2O_4$/CNPs nanocomposites. Due to the facile preparation method of Cr—Ca and abundancy of waste pyrolysis gas, the method is easily scalable for mass production. Since electrochemical properties of $CaCr_2O_4$ containing materials has not been previously investigated, electrochemical characterization of the prepared $CaCr_2O_4$/CNPs nanocomposite was carried out.

**Table 2**
Decomposition of $C_{6+}$ hydrocarbons over Cr—Ca (700 °C).

| No. | Retention time (min) | Identified hydrocarbon[a] | Decomposition (%)[b] |
|---|---|---|---|
| 1 | 2.735 | 1-Methyl-1,3-cyclopentadiene | 44 |
| 2 | 2.802 | 3-Vinyl-1-cyclobutene | 50 |
| 3 | 2.900 | 4-Methyl-cyclopentene | 19 |
| 4 | 3.052 | Benzene | 0 |
| 5 | 3.183 | 1,3- and 1,4-cyclohexadienes | 21 |
| 6 | 3.356 | Cyclohexene | 11 |
| 7 | 3.728 | Unidentified | 85 |
| 8 | 5.044 | Toluene $d_8$ | N.A.[c] |
| 9 | 5.128 | Toluene | 0 |
| 10 | 6.422 | Unidentified | 69 |
| 11 | 6.532 | Unidentified | 100 |
| 12 | 7.162 | Ethylbenzene | 69 |
| 13 | 7.319 | p-Xylene | 52 |

[a] Identification was carried out using reference spectra in GC–MS library.
[b] Calculated based on the areas of peaks of hydrocarbons.
[c] Not applicable.

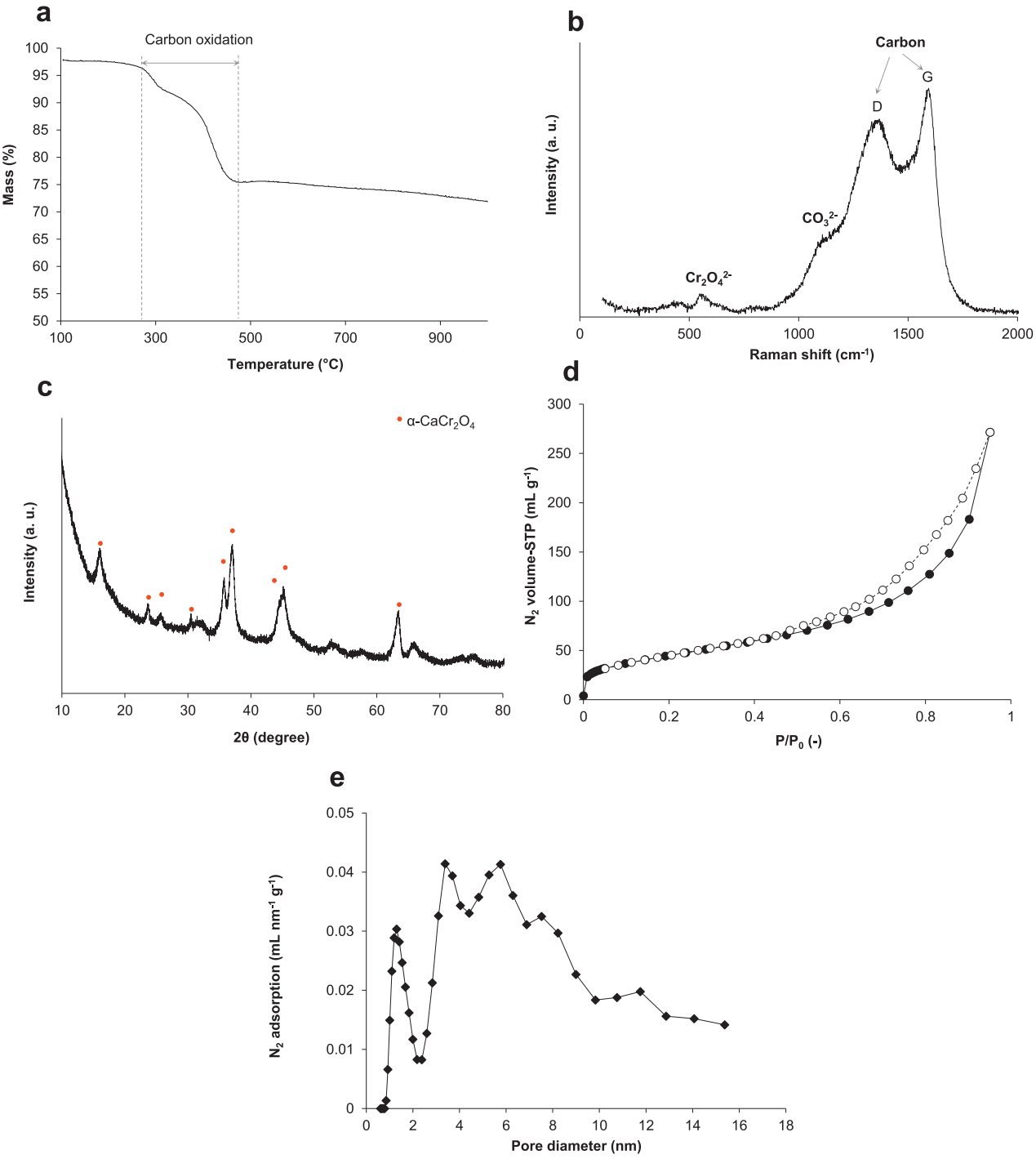


**Fig. 3.** (a) Temperature programmed oxidation profile, (b) Raman spectrum, (c) XRD pattern, (d) $N_2$ adsorption and desorption isotherms and (e) pore size distribution of the nanocomposite synthesized at 700 °C.

### 3.3. Electrochemical properties

Fig. 5a and b show the redox behavior of $CaCr_2O_4$/CNPs deposited on a GC electrode surface characterized by CV and EIS measurements using $Fe(CN)_6^{3-}/^{4-}$ redox couple as a standard probe. In Fig. 5a, the comparison between CVs of bare GC (black curve) and $CaCr_2O_4$/CNPs-modified GC (red curve) electrodes is shown. The CV of $CaCr_2O_4$/CNPs is characterized with a cathodic peak at 0.184 V and an anodic peak at 0.283 V, corresponding to the reduction of $Fe(CN)_6^{3-}$ to $Fe(CN)_6^{4-}$ and the oxidation of $Fe(CN)_6^{4-}$ to $Fe(CN)_6^{3-}$, respectively. The $CaCr_2O_4$/CNPs-modified GC electrode exhibited narrowed peak to peak separation ($\Delta E_{pp}$), where it decreased from 0.124 to 0.099 V in $CaCr_2O_4$/CNPs as compared to GC, indicating better reversibility of heterogeneous electron transfer [34]. Furthermore, the comparison of the magnitude of the anodic and cathodic peak current densities of the bare GC and $CaCr_2O_4$/CNPs-modified GC electrodes clearly shows that the $CaCr_2O_4$/CNPs-modified GC electrode is characterized with higher redox current density, confirming improved heterogeneous electron transfer. Moreover, the higher charging density observed throughout the entire potential range (−0.2–0.6 V) shows the emerged electrochemical double layer capacitive behavior of $CaCr_2O_4$/CNPs-GC electrodes. EIS measurements (Fig. 5b) support the CV results showing decreased resistance of

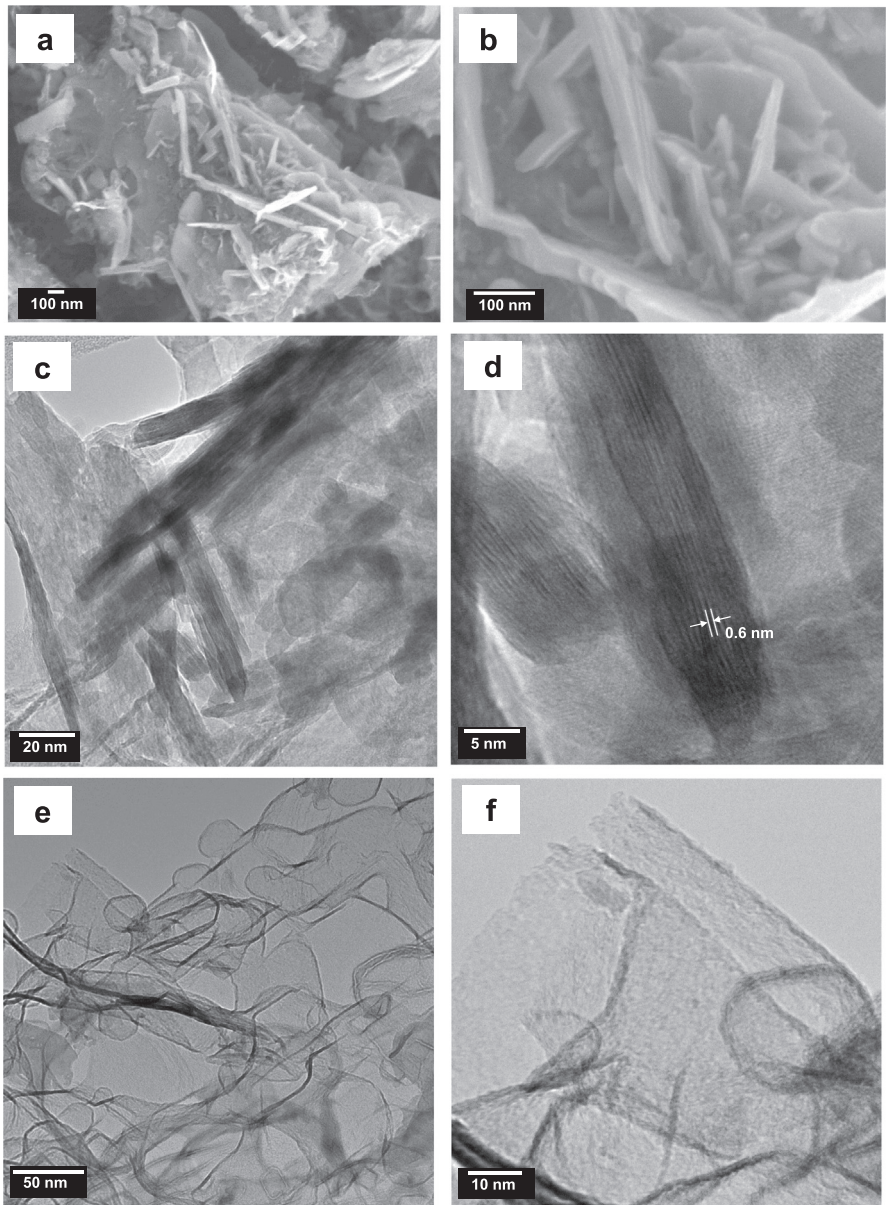


**Fig. 4.** FESEM (a, b) and TEM (c–f) images of the prepared $CaCr_2O_4$/CNPs composite (700 °C).

heterogeneous electron transfer. Specifically, the Nyquist plot exhibits a lowered hemi-circle at a high frequency range, and accordingly, its extrapolation to $Z_{real}$ axis gives a smaller value in the intercept (red curve). It is well known that a hemi-circle size at high frequency range represents the heterogeneous electron transfer kinetics between an electrode surface and redox reactant in a solution phase, and its extrapolation to the $Z_{real}$ axis towards lower frequency range gives the sum of electron transfer resistance and electrolyte/system resistance [35]. The above qualitative electrochemical characterization shows a great prospect of $CaCr_2O_4$/CNPs to be used as a platform for electrochemical sensors, e.g. for hydrogen peroxide determination, with improved sensing characteristics as carbon nanotube films were previously been found offering efficient heterogeneous electron transfer for detection of hydrogen peroxide at low working potential [36]. In addition to the standard characterization of redox behavior, $CaCr_2O_4$/CNPs-modified electrodes were also tested for the oxygen reduction reaction (ORR). Fig. 5c shows ORR over the bare GC electrode (black curve), the GC electrode modified with $CaCr_2O_4$/CNPs (red curve), and GC electrode modified with $CaCr_2O_4$ (blue curve) after calcination of $CaCr_2O_4$/CNPs in air that was used to remove carbon. During the LSV measurements, the electrodes were submerged in air-saturated 0.1 M KOH solution. In the reference experiments, $N_2$-saturated 0.1 M KOH was used in order to ensure that the observed reduction peak occurred due to the ORR. It can be seen that during the ORR, both bare GC and $CaCr_2O_4$-modified GC electrodes demonstrated overpotential of −0.38 V vs Ag/Ag/KCl (sat.) at a similar current density, namely in the range of 0.040–0.043 mA $cm^{-2}$. $CaCr_2O_4$/CNPs-modified electrode showed reduced overpotential of −0.27 V vs Ag/Ag/KCl (sat.) at higher current density, that is 0.050 mA $cm^{-2}$. To compare the obtained results with the best known electrocatalyst for ORR, that is Pt, a commercial 20 wt % Pt on graphitized carbon (C/Pt) (yellow curve) was employed as a working electrode in ORR. C/Pt electrode expressed an onset potential of −0.09 V and a plateau current density of 0.068 mA $cm^{-2}$. Although, the performance of the commercial Pt electrocatalyst clearly outperformed the synthesized $CaCr_2O_4$/CNPs, yet the replacement of expensive Pt electrode by waste-derived carbon nanocomposites as an electrode material for electrocatalysis of ORR for application in fuel cells, is rather desirable.

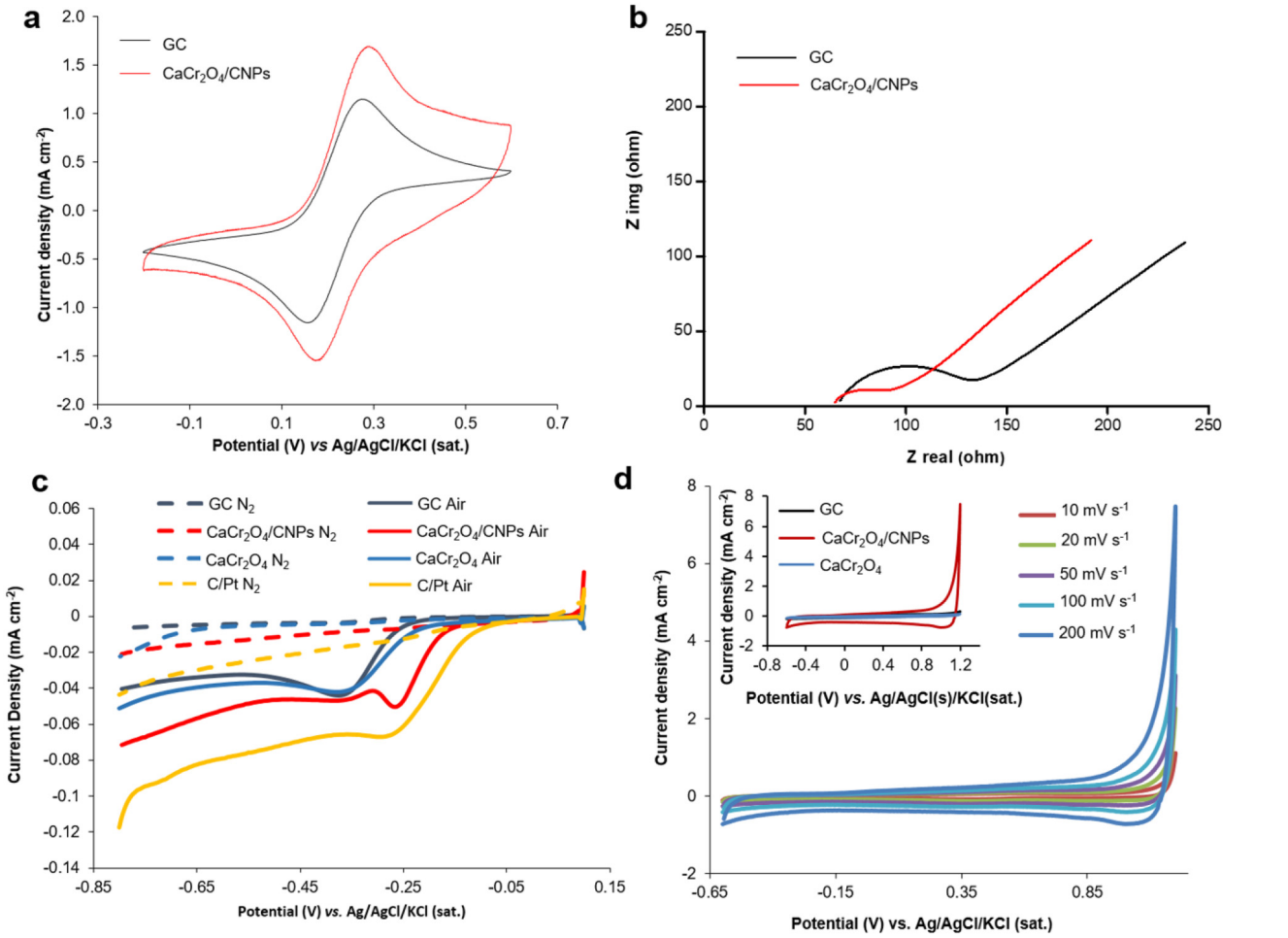


**Fig. 5.** (a) CVs of bare GC (black curve) and $CaCr_2O_4$/CNPs-modified GC (red curve) in 5 mM $Fe(CN)_6^{3-/4-}$ containing 0.1 M KCl. Scan rate: 50 mV $s^{-1}$, (b) Nyquist plots of EIS measurement of bare GC (black curve) and $CaCr_2O_4$/CNPs-modified GC (red curve) in 10 mM $Fe(CN)_6^{3-/4-}$ containing 0.1 M KCl. The frequency range used from 0.1 Hz to 100 kHz at an open circuit potential with an alternating current amplitude of 10 mV, (c) ORR of respective different surfaces in air or $N_2$ saturated 0.1 M KOH, (d) CVs of $CaCr_2O_4$/CNPs at different scan rates in 1 M $H_2SO_4$. Inset: CVs of bare GC, $CaCr_2O_4$- and $CaCr_2O_4$/CNPs-modified electrodes at scan rate of 200 mV $s^{-1}$ in 1 M $H_2SO_4$.

CV measurements shown in Fig. 5a suggest the electrochemical capacitive nature of $CaCr_2O_4$/CNPs-modified GC electrode compared to the bare GC electrode. Since electrochemical double layer capacitance is not a Faradaic (redox) process and charging current is directly proportional to a potential scan speed, the series of CVs were performed using a wider potential range in acidic 1 M $H_2SO_4$ solution in the absence of redox couple at potential scan rates from 10 to 200 mV $s^{-1}$. The inset of Fig. 5d shows that both bare GC and $CaCr_2O_4$-modified GC electrodes exhibit no significant electrochemical capacitive behavior. Whereas for $CaCr_2O_4$/CNPs-modified GC electrodes, a significant charging current indicated an electrochemical capacitance nature. Moreover, some electrochemical pseudocapacitative behavior was also demonstrated since an oxidation peak was observed starting from 0.85 to the maxima at 1.2 V and a consequent reduction peak at 1 V. Previously, chromium oxide-type materials were used as electrodes in electrochemical supercapacitors in aqueous systems [21,37–42]. However, the efficiency of $CaCr_2O_4$ containing composites has not been investigated. When increasing the potential scan rate, the charging current density increased accordingly as expected for a double layer electrochemical capacitor (Fig. 5d). Obviously, the inclusion of a conductive carbon additive is necessary for the composite to exhibit good electrochemical capacitance [21,37,38]. Consequently, the composite material of $CaCr_2O_4$/CNPs was used in charge/discharge experiments to quantify its electrochemical capacitance as it qualitatively demonstrated good electrochemical capacitance performance. Various charge and discharge rates were chosen with a current density ranging from 1 A $g^{-1}$ to 20 A $g^{-1}$ to perform charge/discharge experiments by chronopotentiometry in 1 M $H_2SO_4$ (Fig. 6a). The potential window of the material was defined to be between −0.6 to 1.2 V vs Ag/AgCl/KCl (sat.) as illustrated by its electrochemical activity during cyclic voltammetry in Fig. 5d, demonstrating the exemplary performance across a wide potential window, while a typical chromium oxide material on carbon support operates within a narrow range [21,37–39]. In a recent work, Chen et al. demonstrated that $Cr_2O_3$/multi-walled carbon nanotubes based electrochemical supercapacitor operated within a limited potential window of −0.05 to 0.45 V in basic media of 1.0 M KOH against standard calomel electrode [38]. Separately, Lota et al. developed a chromium oxide-MWCNT electrochemical supercapacitor in acidic media with a relatively small potential window of 0 to 0.8 V in a 2 electrode system in 1.0 M $H_2SO_4$ [21]. An operation of a wide potential window is needed to achieve higher energy-density capabilities of the electrodes [43,44]. As such, the $CaCr_2O_4$/CNPs nanocomposite demonstrates promising behavior as an electrochemical supercapacitor in acidic media with a wide potential window of −0.6 to 1.2 V.

With increasing charge and discharge rates, the time for completion of 1 cycle decreases, as the charges are stored and then eventually expended at a faster rate. The response shows a non-ideal triangular shape due to a redox process, which is a typical electrochemical pseudocapacitance characteristic [45]. From the discharge curve, the corresponding electrochemical capacitance of the material was calculated using Eq. (1). At a discharge rates of 1, 2 and 5 A $g^{-1}$, the electrochemical capacitance of $CaCr_2O_4$/CNPs was maintained at relatively

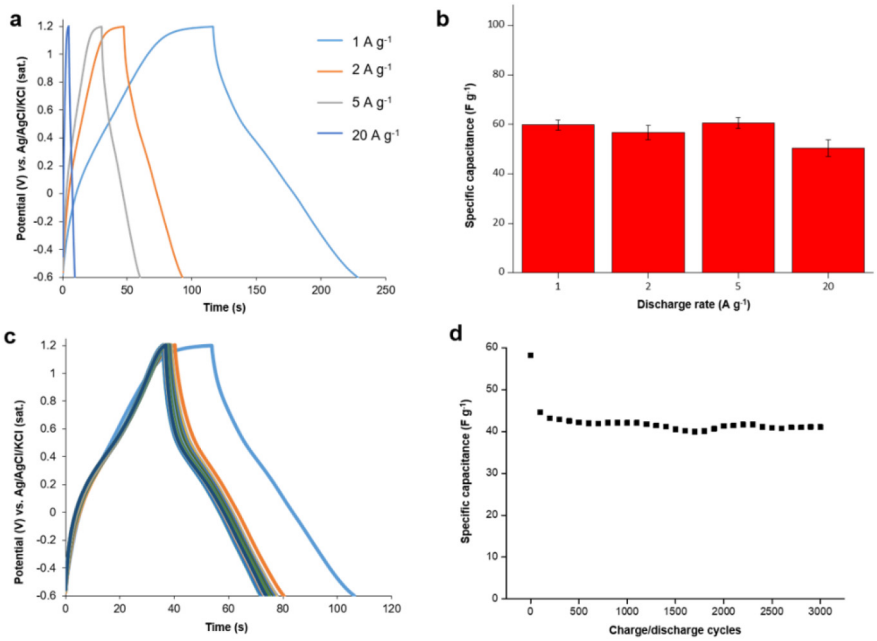


**Fig. 6.** (a) Galvanostatic charge/discharge curves at different current rates of $CaCr_2O_4$/CNPs, (b) average specific electrochemical capacitances of $CaCr_2O_4$/CNPs at different discharge rates (error bar represent standard deviation from 3 readings), (c) long-term charge/discharge of $CaCr_2O_4$/CNPs at 2 A $g^{-1}$, (d) electrochemical capacitance retention and the round trip efficiency at 2 A $g^{-1}$ during 3000 cycles for $CaCr_2O_4$/CNPs. Electrolyte: 1 M $H_2SO_4$.

constant values of 60, 58 and 61 F $g^{-1}$, respectively (Fig. 6b). This is higher than the electrochemical capacitance of 50 F $g^{-1}$ reported for a composite containing $Cr_2O_3$ and single walled carbon nanotubes at charge/discharge rate of 5 A $g^{-1}$ [21]. In case of $CaCr_2O_4$/CNPs, the specific electrochemical capacitance of 50 F $g^{-1}$ was maintained at the charge/discharge rate as high as 20 A $g^{-1}$ (Fig. 6b), demonstrating the superior performance of the synthesized composite over other available chromium-based electrode materials. Besides the better performance, one advantage of $CaCr_2O_4$/CNPs is the simple and scalable synthesis method, which allows for the mass production of inexpensive nanocomposite for energy application as compared to single walled carbon nanotubes. A long term-charge/discharge of the electrode material for 3000 cycles at 2 A $g^{-1}$ was used to determine the stability of the material at long-term cycling (Fig. 6c and d). Apart from the decrease in the electrochemical capacitance from 58 F $g^{-1}$ to 45 F $g^{-1}$ for the initial 100 cycles, the electrochemical capacitance of the $CaCr_2O_4$/CNPs remained relatively stable (i.e. between 40 and 45 F $g^{-1}$), demonstrating the capability of electrode to sustain long-term charge/discharge cycling and reversibility.

## 4. Conclusions

A novel nanocomposite consisting of α-$CaCr_2O_4$ spinel plates bonded with CNPs ($CaCr_2O_4$/CNPs) was produced from mixed plastics using a two-stage pyrolysis and chemical vapor deposition process. The nanocomposite was characterized using CV and EIS measurements, showing that the electrochemical performance of material was related to synergistic interactions between two components (i.e. α-$CaCr_2O_4$ and CNPs). The nanocomposite was applied as an electrocatalyst for ORR and as an electrode material for charge storage. During ORR in alkaline electrolyte, $CaCr_2O_4$/CNPs demonstrated electrocatalytic ability, increasing current density and decreasing overpotential. Furthermore, $CaCr_2O_4$/CNPs exhibited the specific electrochemical capacitance as high as 60 F $g^{-1}$ at 2 A $g^{-1}$ and presented 67% long-term cycling stability over 3000 cycles. High electrochemical capacitance values for $CaCr_2O_4$/CNPs were maintained over a wide potential window of 1.8 V, indicating the suitability of material for the application as an electrode material for charge storage in electrochemical supercapacitors.

## Acknowledgements

The authors would like to acknowledge the Nanyang Environment and Water Research Institute, Nanyang Technological University (Singapore) and Economic Development Board (Singapore) for financial support of this research.

## Appendix A. Supplementary data

Supplementary data to this article can be found online at https://doi.org/10.1016/j.jelechem.2019.113368.

## References

[1] Q. Cheng, J. Tang, J. Ma, H. Zhang, N. Shinya, L.-C. Qin, Graphene and carbon nanotube composite electrodes for supercapacitors with ultra-high energy density, Phys. Chem. Chem. Phys. 13 (2011) 17615–17624.
[2] V.C. Lokhande, A.C. Lokhande, C.D. Lokhande, J.H. Kim, T. Ji, Supercapacitive composite metal oxide electrodes formed with carbon, metal oxides and conducting polymers, J. Alloy Compd. 682 (2016) 381–403.
[3] T. Kou, B. Yao, T. Liu, Y. Li, Recent advances in chemical methods for activating carbon and metal oxide based electrodes for supercapacitors, J. Mater. Chem. A 5 (2017) 17151–17173.
[4] D. Yang, M. I. Ionescu, 8-Metal oxide-carbon hybrid materials for application in supercapacitors, In Metal Oxides, edited by D.P. Dubal and P. Gomez-Romero, Elsevier, 2017, pp. 193–218, Metal Oxides in Supercapacitors, ISBN 9780128111697, https://doi.org/10.1016/B978-0-12-810464-4.00008-5.
[5] H. Osgood, S.V. Devaguptapu, H. Xu, J. Cho, G. Wu, Transition metal (Fe, Co, Ni, and Mn) oxides for oxygen reduction and evolution bifunctional catalysts in alkaline media, Nano Today 11 (2016) 601–625.
[6] Y. Wang, J. Li, Z. Wei, Transition-metal-oxide-based catalysts for the oxygen reduction reaction, J. Mater. Chem. A 6 (2018) 8194–8209.
[7] E.H. Majlan, D. Rohendi, W.R.W. Daud, T. Husaini, M.A. Haque, Electrode for proton exchange membrane fuel cells: a review, Renew. Sust. Energ. Rev. 89 (2018) 117–134.
[8] D. Banham, S. Ye, K. Pei, J. Ozaki, T. Kishimoto, Y. Imashiro, A review of the stability and durability of non-precious metal catalysts for the oxygen reduction reaction in proton exchange membrane fuel cells, J. Power Sources 285 (2015) 334–348.
[9] J. Zhang, X. Bai, T. Wang, W. Xiao, P. Xi, J. Wang, D. Gao, J. Wang, Bimetallic nickel cobalt sulfide as efficient electrocatalyst for Zn–air battery and water splitting, Nano-Micro Lett. 11 (2019) 2.
[10] Y. Li, J. Lu, Metal–air batteries: will they be the future electrochemical energy storage device of choice? ACS Energy Lett. 2 (2017) 1370–1377.
[11] X. Xu, J. Gao, W. Hong, Ni-based chromite spinel for high-performance supercapacitors, RSC Adv. 6 (2016) 29646–29653.

[12] Z. Shahnavaz, S.B.A. Hamid, Fabrication of a novel metal chromite–carbon nanotube composite for the highly efficient electrocatalytic reduction of hydrogen peroxide, Appl. Surf. Sci. 407 (2017) 379–385.
[13] M. Al-Mamun, X. Su, H. Zhang, H. Yin, P. Liu, H. Yang, D. Wang, Z. Tang, Y. Wang, H. Zhao, Strongly coupled $CoCr_2O_4$/carbon nanosheets as high performance electrocatalysts for oxygen evolution reaction, Small 12 (2016) 2866–2871.
[14] Q. Zhou, J. Wang, R. Zheng, Y. Gong, J. Lin, One-step mild synthesis of Mn-based spinel $Mn^{II}Cr_2^{III}O_4$/$Mn^{II}Mn_2^{III}O_4$/C and Co-based spinel $CoCr_2O_4$/C nanoparticles as battery-type electrodes for high-performance supercapacitor application, Electrochim. Acta 283 (2018) 197–211.
[15] J. Aguado, D.P. Serrano, J.M. Escola, Fuels from waste plastics by thermal and catalytic processes: a review, Ind. Eng. Chem. Res. 47 (2008) 7982–7992.
[16] S.L. Wong, N. Ngadi, T.A.T. Abdullah, I.M. Inuwa, Current state and future prospects of plastic waste as source of fuel: a review, Renew. Sustainable Energy Rev. 50 (2015) 1167–1180.
[17] J. Scheirs, Overview of commercial pyrolysis processes for waste plastics, in: J. Scheirs, W. Kaminsky (Eds.), Feedstock Recycling and Pyrolysis of Waste Plastics: Converting Waste Plastics Into Diesel and Other Fuels, John Wiley & Sons 2006, pp. 383–433.
[18] A.V. Neimark, Y. Lin, P.I. Ravikovitch, M. Thommes, Quenched solid density functional theory and pore size analysis of micro-mesoporous carbons, Carbon 47 (2009) 1617–1628.
[19] J. Tkac, J.W. Whittaker, T. Ruzgas, The use of single walled carbon nanotubes dispersed in a chitosan matrix for preparation of a galactose biosensor, Biosens. Bioelectron. 22 (2007) 1820–1824.
[20] M. Maharjan, M. Ulaganathan, V. Aravindan, S. Sreejith, Q. Yan, S. Madhavi, J.-Y. Wang, T.M. Lim, Fabrication of high energy Li–ion capacitors from orange peel derived porous carbon, Chemistry Select 2 (2017) 5051–5058.
[21] G. Lota, E. Frackowiak, J. Mittal, M. Monthioux, High performance supercapacitor from chromium oxide-nanotubes based electrodes, Chem. Phys. Lett. 434 (2007) 73–77.
[22] M.A. Vuurman, F.D. Hardcastle, I.E. Wachs, Characterization of CrO3/Al2O3 catalysts under ambient conditions: influence of coverage and calcination temperature, J. Mol. Catal. 84 (1993) 193–205.
[23] A.M. Rao, E. Richter, S. Bandow, B. Chase, P.C. Eklund, K.A. Willams, et al., Diameter-selective Raman scattering from vibrational modes in carbon nanotubes, Science 275 (1997) 187–191.
[24] J. Gong, B. Michalkiewicz, X. Chen, E. Mijowska, J. Liu, Z. Jiang, X. Wen, T. Tang, Sustainable conversion of mixed plastics into porous carbon nanosheets with high performances in uptake of carbon dioxide and storage of hydrogen, ACS Sustain. Chem. Eng. 2 (2014) 2837–2844.
[25] L. Shi, K. Chen, R. Du, A. Bachmatiuk, M.H. Rümmeli, K. Xie, Y. Huang, Y. Zhang, Z. Liu, Scalable seashell-based chemical vapor deposition growth of three-dimensional graphene foams for oil-water separation, J. Am. Chem. Soc. 138 (2016) 6360–6363.
[26] N. Arnaiz, I. Martin-Gullon, R. Font, M.F. Gomez-Rico, Production of bamboo-type carbon nanotubes doped with nitrogen from polyamide pyrolysis gas, J. Anal. Appl. Pyrolysis 130 (2018) 52–61.
[27] S. Gunasekaran, G. Anbalagan, S. Pandi, Raman and infrared spectra of carbonates of calcite structure, J. Raman Spectrosc. 37 (2006) 892–899.
[28] M.E. Valentine, S. Koohpayeh, M. Mourigal, T.M. McQueen, C. Broholm, N. Drichko, S.E. Dutton, R.J. Cava, T. Birol, H. Das, C.J. Fennie, Raman study of magnetic excitations and magnetoelastic coupling in α-$SrCr_2O_4$, Phys. Rev. B 91 (2015), 144411.
[29] S. Zhai, Y. Yin, S.R. Shieh, S. Shan, W. Xue, C.-P. Wang, K. Yang, Y. Higo, High-pressure X-ray diffraction and Raman spectroscopy of $CaFe_2O_4$-type β-$CaCr_2O_4$, Phys. Chem. Minerals 43 (2016) 307–314.
[30] H. Hu, M. Shi, Y. Yang, H. Liu, M. Xu, J. Shen, H. Yao, Further insight into the formation and oxidation of $CaCr_2O_4$ during solid fuel combustion, Environ. Sci. Technol. 52 (2018) 2385–2391.
[31] A. Rahman, M. Ahmed, Dehydrogenation of propane over chromia/alumina: a comparative characterization study of fresh and spent catalysts, Stud. Surf. Sci. Catal. 100 (1996) 419–426.
[32] Z.Q. Li, C.J. Lu, Z.P. Xia, Y. Zhou, Z. Luo, X-ray diffraction patterns of graphite and turbostratic carbon, Carbon 45 (2007) 1686–1695.
[33] R.I. Jafri, N. Rajalakshmi, S. Ramaprabhu, Nitrogen doped graphene nanoplatelets as catalyst support for oxygen reduction reaction in proton exchange membrane fuel cell, J. Mater. Chem. 20 (2010) 7114–7117.
[34] R.L. McCreery, Advanced carbon electrode materials for molecular electrochemistry, Chem. Rev. 108 (2008) 2646.
[35] A.J. Bard, L.R. Faulkner, Electrochemical Methods: Fundamentals and Applications, 2nd edition John Wiley & Sons, Inc., 2000 386.
[36] J. Tkac, T. Ruzgas, Dispersion of single walled carbon nanotubes. Comparison of different dispersing strategies for preparation of modified electrodes toward hydrogen peroxide detection, Electrochem. Communications 8 (2006) 899–903.
[37] P.M. Kharade, J.V. Thombare, S.L. Kadam, S.B. Kulkarni, D.J. Salunkhe, Layered PPy/$Cr_2O_3$ as a supercapacitor electrode with improved electrochemical performance, J. Mater. Sci. Mater. Electron. 28 (2017), 17908.
[38] B. Chen, Y. Wang, C. Li, L. Fu, X. Liu, Y. Zhu, L. Zhang, Y. Wu, A $Cr_2O_3$/MWCNTs composite as a superior electrode material for supercapacitor, RSC Adv. 7 (2017) 25019–25024.
[39] X. Xu, J. Wu, N. Yang, H. Na, L. Li, J. Gao, $Cr_2O_3$: a novel supercapacitor electrode material with high capacitive performance, J. Mater. Lett. 142 (2015) 172–175.
[40] P. Asen, S. Shahrokhian, Ternary nanostructures of $Cr_2O_3$/graphene oxide/conducting polymers for supercapacitor application, J. Electroanal. Chem. 823 (2018) 505–516.
[41] P.M. Kharade, S.G. Chavan, S.S. Mane, P.B. Joshi, D.J. Salunkhe, Characterization of microwave-sintered barium strontium titanate nanoparticles prepared by the hydrothermal method, J. Chinese Adv. Mater. Soc. 4 (2016) 1–10.
[42] J. Zhu, Y. Jiang, Z. Lu, C. Zhao, L. Xie, L. Chen, J.J. Duan, Single-crystal $Cr_2O_3$ nanoplates with differing crystalinities, derived from trinuclear complexes and embedded in a carbon matrix, as an electrode material for supercapacitors, Colloid Interface Sci. 498 (2017) 351–363.
[43] B.K. Kim, S. Sy, A. Yu, J. Zhang, Electrochemical supercapacitors for energy storage and conversion, in: J. Yan (Ed.), Handbook of Clean Energy Systems 2015, pp. 1–25, https://doi.org/10.1002/9781118991978.hces112.
[44] A. Burke, R&D considerations for the performance and application of electrochemical capacitors, Electrochim. Acta 53 (2007) 1083–1091.
[45] G.Z. Chen, Understanding supercapacitors based on nano-hybrid materials with interfacial conjugation, Progress in Natural Science: Materials International 23 (2013) 245–255.